Chapter 2
Experimental methods and Characterization Techniques

2.1 Introduction

Spinel oxides can be synthesized by several synthesis techniques such as combustion, thermal decomposition, co-precipitation, sol-gel, hydrothermal, etc. as disscussed earlier. These different synthesis methods may produce the spinel oxides with same/different phase, stoichiometry, and microstructure (shape and size) depending upon the synthesis parameter and precursor used. So, the selection of synthesis method is an important step to achieve the required properties. In the present work, a facile and cost-effective co-precipitation method is adopted to synthesize the $Co_xMn_{3-x}O_4$ (x = 1.00 to 2.00) and Cr doped $CoMn_2O_4$ nanoparticles which is discussed in section 2.2. The working principle and operational details of different characterization techniques are discussed in section 2.3.

2.2 Co-precipitation technique

The co-precipitation method is one of the chemical routes with greater control over the chemical homogeneity due to the molecular level of mixing of reactants at low synthesis temperature[133]. It is a cost-effective, simple method and offers different synthesis parameters like control of pH of precipitation, reaction temperature, *etc.* The co-precipitation method consists of several steps such as mixing metal salt solution, precipitation, filtration, washing, drying, and finally calcination. Among these steps, the precipitation is the most significant as the basic properties of final particles are established during this step [133]. There are three major parts of the precipitation step which are nucleation, crystal growth and the aggregation of primary precipitated particles. Mostly both nucleation and crystal growth occur simultaneously, though they can be

performed separately. Clusters larger than the critical size tend to grow further, whereas smaller clusters will redissolve.

In the present work $Co_xMn_{3-x}O_4$ (x = 1.00, 1.25,1.50,1.75, and 2.00) nanoparticles were synthesized using the conventional coprecipitation method. Cobalt nitrate hexahydrate $Co(NO_3)_2.6H_2O$ (Merck, 99%) and manganese chloride tetrahydrate $MnCl_2.4H_2O$ (Merck, 98%) were used as cobalt and manganese precursor. Required amount of precursors were dissolved in double distilled water in particular Co and Mn ratio of 1.00: 2.00, 1.25:1.75, 1.50:1.50, 1.75:1.25, and 2.00:1.00 for x = 1.00, 1.25, 1.50, 1.75 and 2., respectively. Continuous stirring of the prepared solution was performed for homogeneity. 0.5 M NaOH solution was dropwise added in the obtained homogenous mixture of salt until the pH reached 9. Subsequently, to complete the reaction, the obtained turbid solution was stirred for 2 h. Further, to eliminate the unreacted entities and achieve a neutral pH of 7, the resulting suspensions were filtered using the Whatman-manufactured filter paper (Grade 1). After filtration, the obtained precipitate was washed with distilled water and ethanol several time to remove the reacted entities. The powder was dried at 80 °C and then calcined in air for two hours at 600 °C at a rate of 5 °C per minute. Finally, the obtained powder of all the compositions was ground and characterized for structural and physical properties. The schematic diagram of preparation of $Co_xMn_{3-x}O_4$ powder sample is shown in **Figure 2.1**.

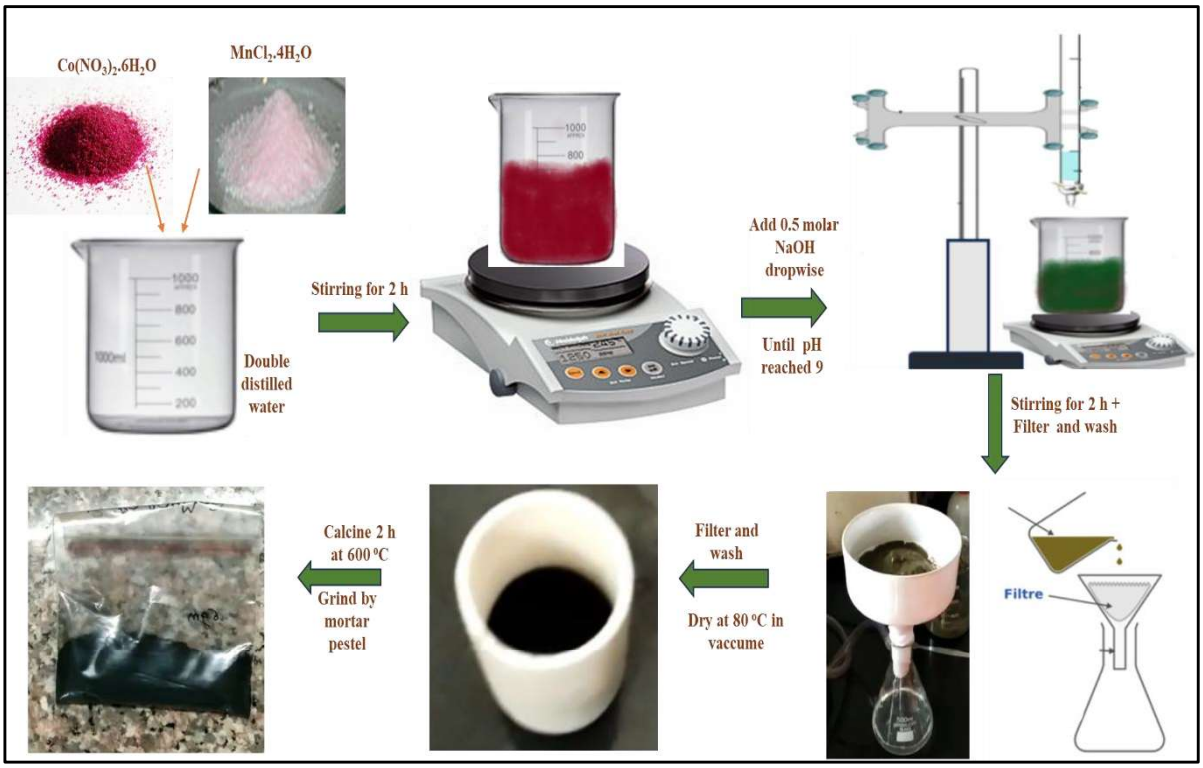

Figure 2.1: A schematic diagram for the synthesis of $Co_xMn_{3-x}O_4$ (x = 1.00, 1.25,1.50,1.75, and 2.00) nanoparticles via a facile co-precipitation technique.

Further Cr doped $CoMn_2O_4$ with varying its concentration was synthesized. $CoCr_xMn_{2-x}O_4$ (x = 0.50 and 1.00) powder prepared by co-precipitation technique from Cobalt nitrate hexahydrate $Co(NO_3)_2.6H_2O$ (Merck, 99%) , manganese chloride tetrahydrate $MnCl_2.4H_2O$ (Merck, 98%), and chromium nitrate nonahydrate $Cr(NO_3)_3.9H_2O$ (Himedia, 98%) precursors. Required amount of these precursors were dissolved in double distilled water in particular Co:Mn:Cr ratio of 1.00: 1.50: 0.50, and 1.00:1.00: 1.00, for x = 0.50 and 1.00, respectively. Continuous stirring of the prepared solution was performed for homogeneity. 0.5 M NaOH solution was dropwise added dropwise in the obtained homogenous mixture of salt until the pH reached 9. Subsequently to complete the reaction, the obtained turbid solution was stirred for 2 h. Further, to eliminate the unreacted entities and achieve a neutral pH of 7, the resulting suspensions were filtered using the Whatman manufactured filter paper (Grade 1). After

filtration obtained precipitate washed with distilled water and ethanol several time to remove the reacted entities. The powder was dried at 80 °C and then calcined in air for two hours at 600 °C and two hours at 1100 °C at a rate of 5 °C per minute. Finally, the obtained powder of all the compositions was ground and characterized for structural and physical properties.

2.3 Characterizations

In order to systematically study the structure, local structure, microstructure and magnetic properties of $Co_xMn_{3-x}O_4$ and Cr doped $CoMn_2O_4$ powder samples, different characterization techniques have been used in the present work. A brief discussion on these characterization techniques is given below.

2.3.1 TGA-DSC

The TGA analysis is a technique employed to check at what temperature the complete phase of material is formed and the thermal durability of materials. This method involves measuring the sample's mass as a function of temperature, allowing for mass changes (such as absorption or desorption), phase transitions, and thermal decomposition. When the sample's mass remains constant within a specific temperature range, it denotes thermal stability in that range. TGA analysis also aids in determining the calcination temperature, acting as an upper limit where the sample starts degrading. Whereas, differential scanning calorimetry (DSC) is a thermal analysis technique used to observe changes in thermal behavior during phase transitions within a system. The difference in the heat required to raise the temperature of the test sample compared to the reference sample is measured, to keep both at the same temperature. The sample material is typically placed in a small capsule made of alumina along with an inert powder like α-Al_2O_3, which doesn't exhibit any heat-related effects. The two capsules are heated at a

constant rate, and the temperature difference is plotted either against time or against specific temperature points within the apparatus. If any changes occur to the test sample, resulting in either release of heat or absorption of heat, the temperature of the sample will increase or decrease compared to the reference sample. This increase or decrease in temperature indicates either process is an exothermic peak or endothermic. On the other hand, the magnitude of the peaks can be used to quantify the amount of heat released or absorbed during the physical or chemical changes [134]. In this thesis work, TGA has been carried out on $CoMn_2O_4$ sample in the temperature range of 30 °C to 800 °C in a nitrogen gas atmosphere to decide the calcination temperature.

2.3.2 X-ray diffraction (XRD)

X-ray diffraction (XRD) is a non-destructive characterization technique which is widely adopted to determine the phase, purity, and the crystal structure of a particular material. This technique works on the famous Bragg's law of diffraction proposed by W. H. Bragg and his son W. L. Bragg. According to Bragg's law, when a monochromatic beam of x-rays incident on a set of equally spaced crystal planes, the constructive interference of the diffracted x-rays could occur only after the fulfillment of the following two conditions. First, the angle of incidence of x-rays must be equal to the diffraction angle. Second, the path difference between the incident and diffracted x-rays must be an integral multiple of the x-ray wavelength. Bragg's law is expressed as

$$2d\sin\theta = n\lambda \qquad (2.1)$$

where, λ is the wavelength of x-ray, d is the inter planer spacing, θ is the angle of incidence, and n represents the order of diffraction. A schematic diagram illustrating Bragg's law is shown in **Figure 2.2**. In a typical diffraction pattern, intense Bragg peaks can be observed at a certain scattering angle where the constructive interference satisfies

Bragg's law. Generally, the number of Bragg peaks in a diffraction pattern depends on the crystal symmetry of the material. A low crystal symmetry such as monoclinic exhibits a large number of Bragg peaks due to numerous lattice planes, whereas high crystal symmetry such as cubic and tetragonal exhibits fewer Bragg peaks due to the limited number of lattice planes in them. Besides the crystal symmetry, the size and shape of particles also affect the nature of Bragg peaks.

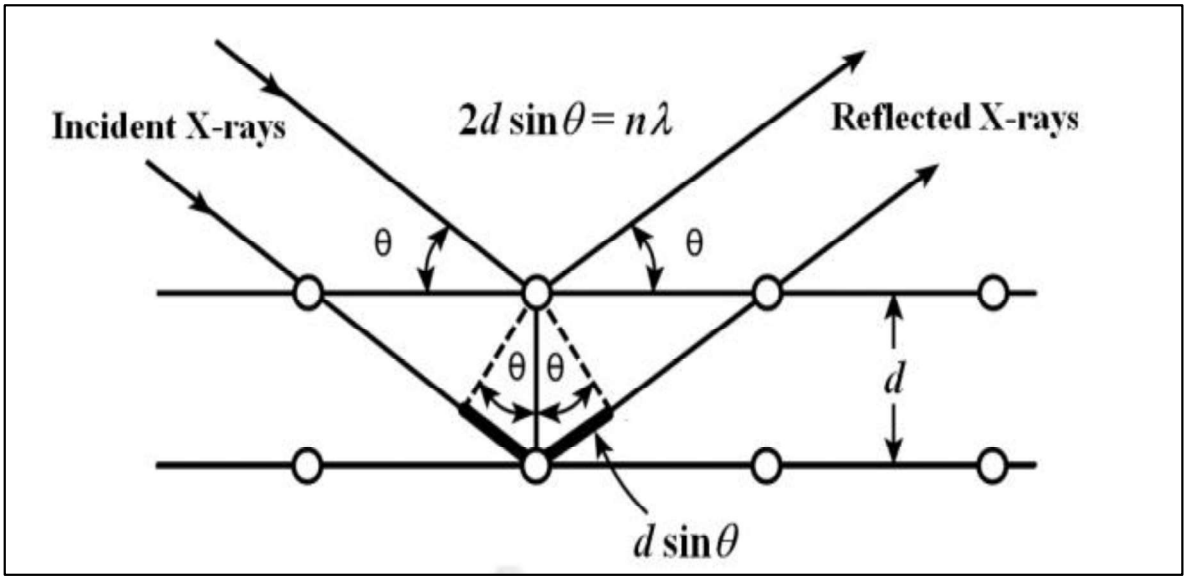

Figure 2.2: A schematic diagram for the Bragg's x-ray diffraction.

In the present thesis, Rigaku Miniflex makes X-ray diffractometer (Cu K_α with λ = 1.54 Å) operating in a Bragg-Brentano geometry was used to acquire the XRD patterns. The x-ray diffractometer was fitted with the graphite monochromator and the x-ray wavelength used was 1.5418 Å. The XRD data was indexed and matched with Joint Committee on Powder Diffraction Standards data (JCPDS) to confirm the phase purity of the samples. The analysis of diffraction patterns was carried out by employing the Rietveld refinement method using the FullProf program [135,136]. Rietveld Refinement probes phase purity of the samples and also gives the crystal structure information such as lattice parameter, atomic position, occupancy, bond length, bond angle, *etc* [137]. Basically, it uses a non-linear least

square method to minimize the difference between the experimental and the calculated XRD patterns. In this method, the background was refined using a polynomial function and a Pseudo-Voigt function was chosen for optimizing the peak shape. Global parameters such as coefficients of background polynomial, scaling factor, FWHM parameters (u, v, w), and the lattice parameters (a, b, c) were mainly varied during the refinement. In addition to the fractional atomic coordinates (x, y, z), isotropic (temperature) displacement parameters and occupancy values were varied. Here, the occupancy is defined as the multiplicity of the Wyckoff position divided by the maximum multiplicity of the same space group. The occupancy of oxygen was taken as 1 and it was not varied throughout the refinement. The reliability factors like R_p (profile factor), R_{wp} (weighted profile factor), R_{exp} (expected weight factor), and χ^2 (reduced chi-square) were used to evaluate the quality of Rietveld refinement. The bond lengths/interatomic distances and bond angles were calculated using the optimized fractional coordinates and lattice parameters by using the Vesta program available in the FullProf suite [135].

2.3.3 X-ray photo electron spectroscopy (XPS)

XPS also peculiarly known as electron spectroscopy for chemical analysis (ESCA) is used for the analysis of the chemical state of the elements. This technique is sensitive at the surface which provides knowledge regarding the composition of the materials, oxidation state of the elements constituting the material and valence band structure by probing the surface of the specimen. The principle of XPS is based on the photoelectric effect. When the sample is irradiated with the monochromatic X-ray photons having energy hν, ejection of electrons takes place from the surface of the sample. Nearby electrons will scatter these photoelectrons, slowing them down and causing them to lose some of their energy. Therefore, photoexcited electrons do not penetrate over the specimen due to high energy loss. This undesirable photoelectron scattering produces

unwanted secondary inelastic background intensity. Due to the high degree of scattering, only photoelectrons originating from a depth of a few tens of angstrom can be identified. The kinetic energy (K.E.) of emitted electrons are given by [138].

$$K.E. = h\nu - B.E. - \Phi \quad (2.2)$$

Where hν represents the energy of the incident X-ray photon, B.E. is the binding energy of the emitted electron and Φ is the work function. From equation 2.2, it is clear that photoelectrons are produced only if hν ≥ B.E. + Φ. The emitted photoelectrons are identified by their respective kinetic energies (KE). Photoelectrons with appropriate KE pass through the work function barrier and reach the detector. In general, when the chamber is evacuated to ultra-high vacuum, scattering and collisions between emitted electrons are reduced. This increases the mean free path of the emitted electrons, allowing them to easily reach the detector. The X-ray photoelectron spectra show the relationship between the frequencies of emitted electrons and their K.E. The energy distribution of electronic states for a given photon energy is referred to as the distribution of kinetic energy of photoelectrons. In the present study, we employed XPS instrument from VSW Al-Kα (energy = 1486.6 eV) radiations. Vacuum level for sample preparation compartment (SPC) was ~ 10-8 Torr and the sample analysis chamber (SAC) was ~ 10-9 Torr. First of all, we scanned over the full energy range (survey scan), and then specifically selected Mn 2*p*, Co 2*p,* and O 1*s* core level spectra for our study. All observed peaks were calibrated to C 1*s* peak at 284.6 eV. XPS data were fitted via software XPS peak 4.1 to find out exact peak positions, oxidation states and the ratio of the elements present with different oxidation state in the sample.

2.3.4 Transmission Electron Microscopy (TEM)

TEM is a powerful technique for probing the structure and morphology including shape, size and distribution of nanoparticles. TEM comprises of a vacuum system, an electron gun electromagnetic lenses, recording devices, high voltage generator, and the associated electronics. The resolution of the modern TEM is under 0.2 nm even with a fair amount of the tilting of the specimen. TEM utilizes electrons with shorter wavelengths, enabling the capture of high-resolution images. A finely focused electron beam, generated by the electron gun assembly and electromagnetic condenser lenses, is accelerated by an anode typically set at 100 keV relative to the cathode. The condenser aperture limits the beam, filtering out uncollimated electrons. The collimated, high-energy electron beam (200 keV and above) interacts with the specimen, scattering based on its thickness and electron transparency. The scattered electrons, which undergo changes in phase and amplitude, are focused by the objective lens to form an image on a phosphor screen or a charge-coupled device (CCD) camera.

TEM operates in two primary modes: diffraction mode and imaging mode. In modern instruments, switching between these modes is achieved by changing the excitation of the lenses located after the objective lens. The well distributed particles of TEM image could be analyzed for shape and size distribution. The histogram of particles distribution (particles size vs. number of particles) is plotted with the help of Image J software. Fitting of the data using Lorantzian distribution provides the average particle size. The selective area electron diffraction (SAED) pattern shows well concentric rings of different radii. The diffraction rings are indexed by calculating inverse of its radii and matching it with inter-planar spacing (d) in reciprocal space of XRD data using WinPLOTR software.

High Resolution Transmission Electron Microscopy (HR-TEM) is the advance version of imaging in TEM, provides the information at atomic scale, with the image of the crystal structure of the sample. The scattered and transmitted beams are used to generate an interference pattern. The phase contrast picture of HRTEM is very small similar to the unit cell in the crystal. It can create images with high resolution below 0.1 Å magnification. The voltage applied for the electron gun is 200 kV. The well distinguished atomic planes of HRTEM were indexed by calculating the interplanar distance and were compared with the XRD data to confirm the crystal structure. Samples were prepared by dispersing 1 milligram of $Co_xMn_{3-x}O_4$ powder in 15 ml of ethanol and sonicated in ultrasonicator for homogeneous mixing. A sonicated solution was dropcasted on the commercial TEM grid (carbon coated copper grid). Further, the grid was dried in vacuum oven to evaporate the ethanol for using in TEM.

2.3.5 Scanning Electron Microscope (SEM)

A scanning electron microscope (SEM) utilizes a focused electron beam to produce images of a sample and a schematic diagram of SEM is shown in **Figure 2.3**. In the SEM, a cathode within the electron gun emits a narrow electron beam, both at low and high energy levels. This feature enhances the spatial resolution of the microscope while minimizing potential charging or damage to the sample. The vacuum is maintained within the microscope. The electron beam passes through electromagnetic lenses and focus on the specimen. This interaction between electron beam and specimen generates various types of electrons. A detector is used to detect secondary electrons, and by comparing the intensities of secondary and primary electrons, an image of the sample surface is formed. The interaction between the electrons and the atom in the sample produces different signals that can be detected and provide information about the morphology and composition of the sample. The electron beam scans the sample in a raster pattern, and

by combining the beam's position with the detected signal, an image is produced [139,140]. In the present work, the image of the material was taken using the Nova Nano SEM 450, FEI Company USA (S.E.A.) PTE, Ltd. conditions.

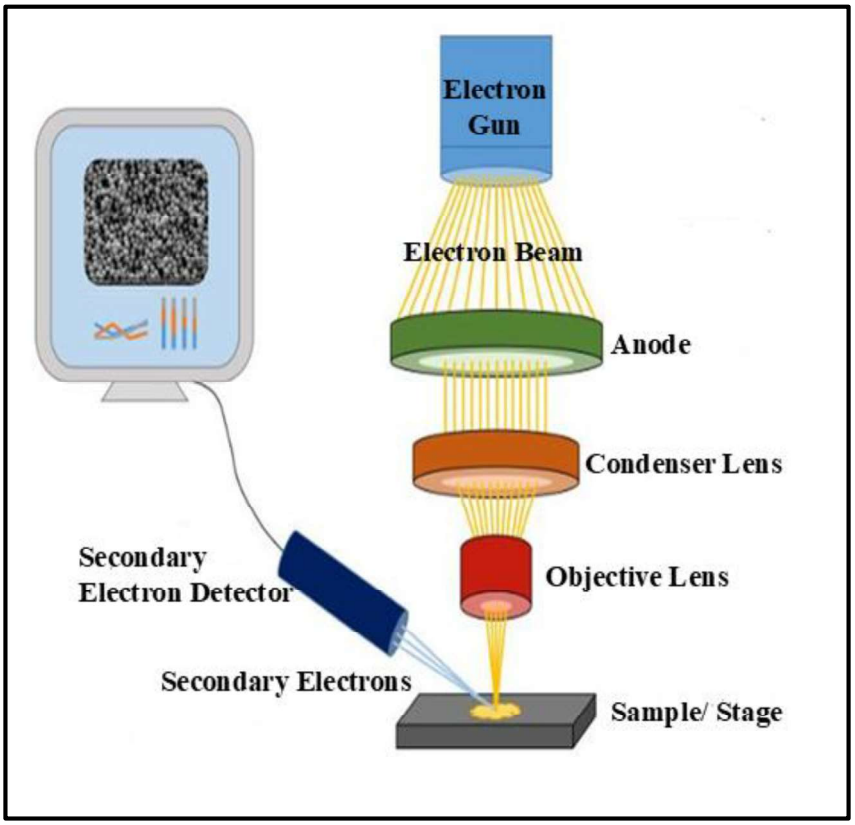

Figure 2.3: Schematic illustration of SEM.

In the present work, samples were coated with the extremely thin layer (1.5 to 3.0 nm) of gold to make the surface electrically conducting. Then, a field emission gun based scanning electron microscope (FE-SEM) of ΣIGMA, ZEISS was used for recording the images of coated samples. A java-based imaging program, ImageJ was used for processing and analyzing the FE-SEM images.

2.3.6 X-ray absorption fine structure (XAFS) spectroscopy

XAFS spectroscopy is an advanced technique to examine the local structure at atomic and molecular scales in crystalline materials, amorphous materials like glasses, liquid solutions, organic materials, quasicrystals, *etc* [141–143]. Therefore, XAFS finds its uses in a variety of research areas such as materials science, synthetic chemistry, structural biology, environmental science, *etc*. In XAFS spectra, the probability of x-ray photon absorption as a function of energy is represented by the absorption coefficient, μ. When the binding energy of a core-electron of an absorbing element exactly matches with the x-ray photon energy, a sudden jump in μ known as the absorption edge is observed. XAFS spectra mainly consist of X-ray Absorption Near Edge Structure (XANES) and Extended X-ray Absorption Fine Structure (EXAFS) regions as shown in **Figure 2.4**.

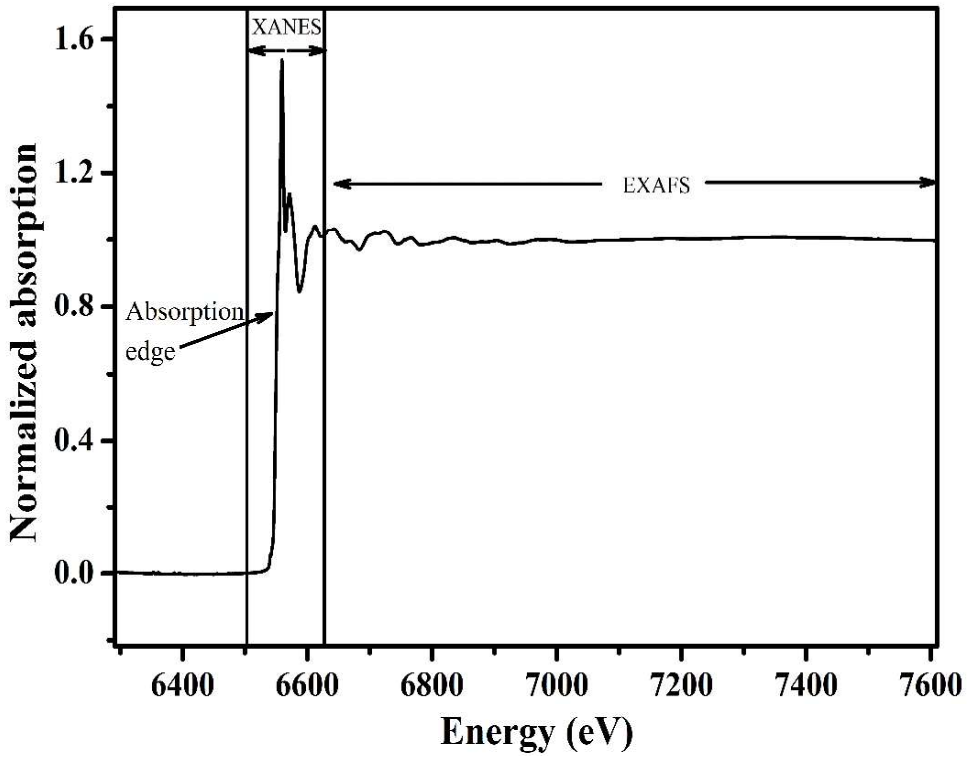

Figure 2.4: A normalizes and background subtracted absorption spectra of $CoMn_2O_4$ measured at Mn K-edge.

Generally, the region lying in the energy range of 30 eV ≤ absorption edge energy, E_0 ≤ 50 eV is called XANES [143]. The shape of the XANES region mainly depends on the intra-atomic electronic transitions and density of states (DOS) just above the Fermi level in the absorbing atom [144]. From XANES, the electronic states and the local geometry surrounding the absorbing atom can be determined [143,144]. The EXAFS region starts from approximately 50 eV above the E_o and it mainly provides information about the bond length (interatomic distance) and types and number of neighboring atoms surrounding the absorbing atom. In EXAFS, the emitted photoelectrons from the absorbing atom propagate as a spherical wave and interact with the incoming wave of backscattered photoelectrons from the neighboring atoms. This interaction results in both constructive and destructive interferences, and consequently, an oscillatory feature is observed in the EXAFS spectra [141]. The relation between the μ, oscillations $\chi(k)$, and the absorption coefficient μ_0 of an isolated atom is given by:

$$\chi(k) = \frac{\mu(k) - \mu_0(k)}{\mu_0(k)} \tag{2.3}$$

XAFS can be performed in three different modes: (i) fluorescence mode where the intensity of fluorescence emitted due to relaxation of core-hole is compared with the intensity of incident x-ray photon; (ii) electron yield mode in which the ejected electron is measured as the core-hole is filled; (iii) transmission mode where the intensity is measured for the incident and transmitted x-ray beam to the sample [145]. The absorbance coefficient μ in the transmission mode is calculated as:

$$\mu(x) = -\ln\left(\frac{I_1}{I_0}\right) \tag{2.4}$$

Where x is the sample thickness. I_0 and I_1 represent the intensity of incident and transmitted x-ray beams. Ionization detectors are used to measure the x-ray intensity. The

detectors are ionization chambers filled with the gas mixture. When the x-ray beam passes through these ionization chambers, it induces a photo ion current of the intensity proportional to that of x-ray beam. The schematic diagram of EXAFS in transmission mode is shown in **Figure 2.5**.

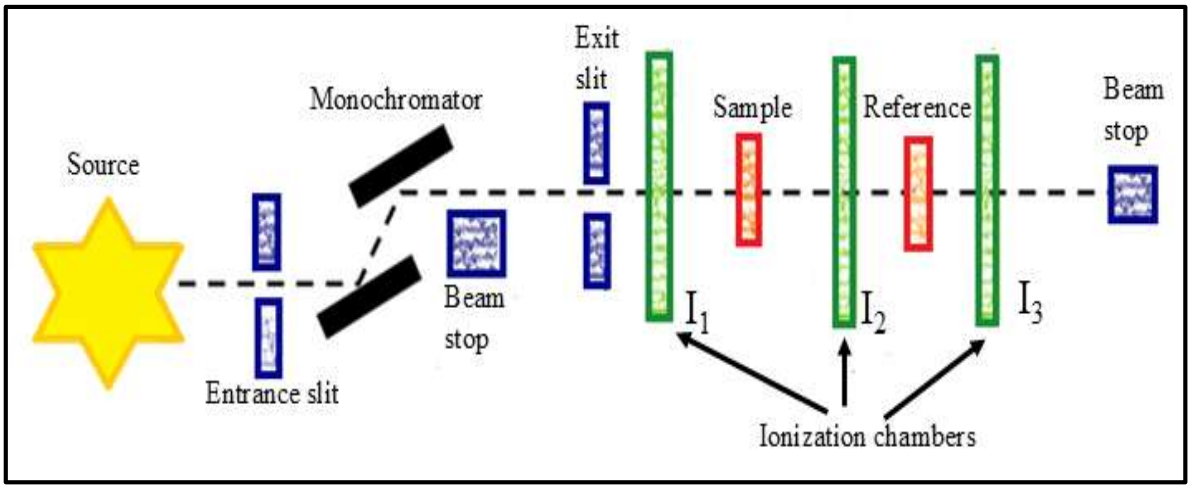

Figure 2.5: A schematic illustration of the EXAFS measurement setup in the transmission mode.

The size and the energy of the x-ray beam from the synchrotron source to the sample is decided by the slits and the monochromators, respectively. In order to calculate the μ, while the sample is placed between chambers I_1 and I_2, the reference sample is placed between chambers I_2 and I_3. The absorption spectra obtained from the reference sample is utilized in calibrating the energy scale of absorption spectra of the measurement sample [145]. For low-temperature measurement of XAFS, the sample needs to be enclosed in a liquid-N_2 or liquid-He cryostat having a window to allow the x-rays to pass.

Demeter [146], EXCURVE, GNXAS, FEFF, FitIT, LARCH [147] *etc.* are the Software packages available for the analysis of EXAFS data. Before starting the EXAFS analysis, the data reduction is performed for extracting the EXAFS spectra out of the raw absorption data. The data reduction includes the following steps:

1. The subtraction of pre-edge and post-edge backgrounds contributing to the absorption spectra.

2. Normalization of the background subtracted absorption spectra between 0 and 1. The normalization is performed so that the final EXAFS spectra can be compared with each other.

3. Determining the absorption energy, E_0 as the energy at which the intensity of normalized spectra is 0.5.

4. Converting the absorption spectra from the energy space to *k* space and then k^n (n = 1, 2, and 3) weighting of $\chi(k)$ spectra.

5. Fourier transformation (FT) of $\chi(k)$ spectra into the *R* space.

Finally, the FT EXAFS spectra is fitted using the theoretical models. The theoretical models are developed using the *ab initio* calculations provided in the analysis software [146]. In a typical fitting, the dimensions of a theoretical model are adjusted so as to optimize the agreement between calculated and experimental EXAFS spectra. The analysis of EXAFS can yield the parameters like coordination number (*N*), absorber-backscatterer distance (*R*), mean-square relative displacement (σ^2), amplitude reduction factor (S_0^2), and Fermi energy position (E_0). While the parameters *N*, σ^2 and S_0^2 affect the amplitude of the oscillations in EXAFS, the phase of the oscillation is affected by E_0 and *R* [141,148]. Typical values for the above-mentioned parameters are the following. The difference between *R* obtained from the fitting and *R* obtained from the theoretical model should not be more than 0.1 Å. *N* must not be negative. σ^2 value should lie between the 0.002 and 0.03 Å^2. S_0^2 can take the value in the range of 0.7 to 1.05. E_0 value should lie between -10 and 10 eV. Two metrics such as EXAFS residual factor (*R*-factor) and statistical factor

(χ_v^2) are used to evaluate the quality of the fit [141]. The *R*-factor defines the fractional mismatch between the experimental and fitted data points as:

$$R = \frac{\sum_{i=1}^{N}(data_i - fit_i)^2}{\sum_{i=1}^{N}(data_i)^2} \tag{2.5}$$

R-factor below 0.02 represents the good agreement between the measured and theoretical spectra and, *R*-factor between 0.02 and 0.05 although denote some disagreement, but is still widely accepted. The χ_v^2 measures the difference between measured and theoretical spectra with respect to the uncertainties in the measured spectra. It is given by:

$$\chi_\nu^2 = \frac{N_{idp}}{\nu N}\sum_{i=1}^{N}\frac{(data_i - fit_i)^2}{\varepsilon_i^2} \tag{2.6}$$

Where

$$\nu = N_{idp} - N_p \tag{2.7}$$

N_{idp} is the total number of data points in the measured spectra. N_p is the total number of parameters optimized during the fitting and ε is the uncertainty present in the measured spectra.

Here, X-ray absorption spectroscopy (XAFS) spectra at Co, Mn and Cr K-edge were taken through the XAS beamline, P-64, PETRA-III, DESY, Hamburg, Germany. The target materials were prepared by thoroughly mixing the calcined powder with cellulose [$(C_6H_{10}O_5)_n$] in the proper ratio and prepared a pellet of 15 mm diameter using one ton of pressure. The room temperature XAS spectra were collected in transmission mode using an ionization chamber filled with a gas mixture of Kr, He, Ar, and N_2. Standard metal foils of Co, Mn, and Cr metal were used to calibrate the energy scale at Co, Mn, and Cr K-edges, respectively, and a fixed-exit monochromator equipped with

Si(111) and Si(311) crystals was utilized to monochromatized the white beam. XANES and EXAFS spectra were recorded at a constant energy step and *k*-step of 0.2 eV and 0.03 $Å^{-1}$, respectively. To enhance the data quality three scans were conducted at each K-edge and averaged. The Demeter package which comprises three programs namely Athena, Artemis, and Hephaestus was utilized to analyze and fit the data [146]. Athena program was employed to process the row data by applying different operations such as background removal, normalization, main K-edge determination, *etc,* by which it convert the raw data into a suitable form. Artemis program was employed to fit the EXAFS spectra utilizing the theoretical standards models by FEFF and ATOMS codes given in it.

2.3.7 Magnetic measurements

The vibrating sample magnetometer (VSM) coupled with the Superconducting Quantum Interference Device (SQUID) has become very successful in measuring the magnetic properties of a wide range of materials. A SQUID VSM magnetometer is a highly sensitive magnetometer that combines the extreme sensitivity of SQUID with the high speed of VSM. Using the VSM, one can measure the DC moment as a function of temperature, magnetic field, and time. A SQUID magnetometer allows measuring the moment as small as 1×10^{-15} Tesla. A SQUID VSM magnetometer mainly consists of the following parts:

a. Superconducting magnet: The most obvious advantage of employing a superconducting magnet is that a large electrical current can flow through it without dissipating the heat. The superconducting magnet is constructed in a completely closed superconducting loop which allows it to perform in the persistent mode. In persistent mode, the superconducting loop is charged with current up to the desired level and then provides a magnetic field during the measurement without employing the external power

source. To change the flowing current or the magnetic field of the magnet in the persistent mode, a persistent-current switch is used which makes a small segment of the closed superconducting loop electrically open, thus allowing the external power supply to change the current flowing in the loop. Once the desired magnetic field is achieved, the loop is closed again and the power supply is cut-off. The niobium-based compounds are commonly used in making superconducting magnets.

b. Sample chamber and holder: The sample is mounted at the holder (quartz or copper made) which is attached at the end of a sample rod. A stepper-motor-coil drives the sample rod into the sample chamber in discrete steps. The sample chamber is generally made in a tube shape and with the help of Helium gas, it is maintained at low pressure. For purging and evacuation purposes, the sample chamber is airlock at the top.

c. Detection coil: The superconducting detection coil is a set of three coils made from the wounding of a single piece of superconducting wire in a second-order gradiometer configuration. It is placed at the center of the superconducting magnet and outside of the sample chamber. When the sample moves through it, the magnetic field associated with the sample couples inductively to the coil. The main purpose of the gradiometer configuration is to reduce the noise level in the detection coil caused by the high magnetic field of the magnet.

d. Superconducting Quantum Interference Device (SQUID): A SQUID is the most sensitive device available in the magnetometer for measuring the magnetic field from the sample. It consists of a closed superconducting loop having Josephson junctions (one or two) in the path of electrical current flowing in the loop. The remarkable features of SQUID derive from the fact that it can detect the moment as small as 10^{-15} Tesla, yet at the same time can work with the field as large as 7 Tesla. Interestingly, sample's magnetic

field is not detected by the SQUID directly. Instead, when the sample passes through the detection coil, the current is induced in the detection coil due to the magnetic moment of the sample. This induced current passes through a superconducting wire to the SQUID. The change in magnetic flux in the detection coil induces a proportional change in the detection coil current. In practice, this variation in flux is brought by vibrating the sample at a fixed frequency under the uniform field. As SQUID works as a highly-linear current to voltage converter, any variation in the detection coil current results in a proportional variation in the SQUID output voltage. The magnetic moment of the sample is proportional to SQUID output voltage. A SQUID in thin-film form is placed below the sample chamber.

In the present work, temperature and field dependent magnetizations of samples are measured using the Magnetic Properties Measurement System (MPMS3) of Quantum Design, USA. The magnetic measurements were performed in the temperature range of $3\ K \leq T \leq 300\ K$ and in the magnetic field range $-6\ Tesla \leq H \leq +6\ Tesla$. Prior to the magnetic measurement, any trapped magnetic flux in the superconducting coil was eliminated by demagnetizing the coil in an oscillatory mode from -60 to +60 kOe at 300 K. Along with this, we have measured M-H loop at FC condition at external magnetic field of 10 kOe and repeated for six cycles for training effect measurement.